Journal of Structural Biology: X 10 (2024) 100111

Contents lists available at ScienceDirect

Journal of Structural Biology: X

journal homepage: www.sciencedirect.com/journal/journal-of-structural-biology-x

Assessment of submicron bone tissue composition in plastic-embedded samples using optical photothermal infrared (O-PTIR) spectral imaging and machine learning

Isha Dev [a], Sofia Mehmood [a], Nancy Pleshko [a], Iyad Obeid [b], William Querido [a,*]

[a] Department of Bioengineering, Temple University, Philadelphia, PA, 19122, USA
[b] Department of Electrical and Computer Engineering, Temple University, Philadelphia, PA 19122, USA

ARTICLE INFO

Edited by Bernhard Ganss

Keywords:
Bone tissue composition
Optical photothermal infrared (O-PTIR) spectroscopy and imaging
Submicron resolution
Machine learning
Bone fragility
Biomineralization

ABSTRACT

Understanding the composition of bone tissue at the submicron level is crucial to elucidate factors contributing to bone disease and fragility. Here, we introduce a novel approach utilizing optical photothermal infrared (O-PTIR) spectroscopy and imaging coupled with machine learning analysis to assess bone tissue composition at 500 nm spatial resolution. This approach was used to evaluate thick bone samples embedded in typical poly(methyl methacrylate) (PMMA) blocks, eliminating the need for cumbersome thin sectioning. We demonstrate the utility of O-PTIR imaging to assess the distribution of bone tissue mineral and protein, as well as to explore the structure-composition relationship surrounding microporosity at a spatial resolution unattainable by conventional infrared imaging modalities. Using bone samples from wildtype (WT) mice and from a mouse model of osteogenesis imperfecta (OIM), we further showcase the application of O-PTIR spectroscopy to quantify mineral content, crystallinity, and carbonate content in spatially defined regions across the cortical bone. Notably, we show that machine learning analysis using support vector machine (SVM) was successful in identifying bone phenotypes (typical in WT, fragile in OIM) based on input of spectral data, with over 86 % of samples correctly identified when using the collagen spectral range. Our findings highlight the potential of O-PTIR spectroscopy and imaging as valuable tools for exploring bone submicron composition.

Introduction

Bone tissue has a fascinating and complex structure, hierarchically organized from the nano to the macroscale in a manner that changes at any length scale can affect the mechanical function and integrity of bone (Buss et al., 2022). At the nano and submicron scales, the hallmark of bone is its mineralized extracellular matrix, composed primarily by apatite (calcium phosphate) mineral nanocrystals, type I collagen fibrils, and water. These form the building blocks of bone structure and integrity: mineralized collagen fibrils and bundles on the scale of ~500 nm (Buss et al., 2022). Many studies with animal models and human bone biopsies have shown that bone tissue-level composition changes with aging, disease states, and different drug treatments (Boskey, 2013; Boskey and Imbert, 2017; Taylor and Donnelly, 2020). Thus, at its most fundamental level, the relative amounts, intrinsic properties, and distribution of matrix components are the drivers of bone tissue quality and strength. For example, changes in relative content of mineral, collagen and water, mineral nanocrystal size, amount of carbonate (CO_3) incorporated in the mineral, and mineral stoichiometry (Ca/P ratio) have all been associated with decreased bone strength with aging and diseases, such as in osteoporosis and osteogenesis imperfecta (OI, or brittle bone disease) (Boskey, 2013; Boskey and Imbert, 2017; Taylor and Donnelly, 2020).

Investigations into bone tissue composition have frequently been pursued by using vibrational spectroscopic techniques, especially Fourier transform infrared (FTIR) and Raman spectroscopy and imaging (Taylor and Donnelly, 2020; Boskey and Camacho, 2007; Querido et al., 2021). These methods have been well established as a label-free tool to assess tissue composition and molecular structure based on vibrations of their chemical bonds (Baker et al., 2014; Balan et al., 2019). These approach allow to simultaneously assess multiple tissue components via their "spectral fingerprint", which comprise diverse absorbance bands that can be used for identifying and quantifying specific tissue components, such as those from bone collagen (Amide I, Amide II, C–H) and

* Corresponding author.
E-mail address: william.querido@temple.edu (W. Querido).

https://doi.org/10.1016/j.yjsbx.2024.100111

Available online 9 October 2024

apatite (PO_4, CO_3) (Taylor and Donnelly, 2020; Boskey and Camacho, 2007; Querido et al., 2021). FTIR and Raman imaging have strengths and weaknesses when compared with each other, which has been reviewed elsewhere (Taylor and Donnelly, 2020; Querido et al., 2021).

An inherent limitation of conventional FTIR imaging is that its spatial resolution is limited to several micrometers (~6–25 μm), which cannot adequately capture properties of tissue features at the submicron scale of the building blocks of bone tissue quality. The relevance of this limitation is illustrated by studies that highlighted the role of submicron scale features in bone strength (Abel et al., 2021; Garcia-Giner et al., 2021; Qian et al., 2020; Sabet et al., 2016; Tai et al., 2007; Zimmermann et al., 2011), including for example as mechanisms in age-related hip fractures (Ma et al., 2020).

A significant advancement in this field was the recent development of optical photothermal infrared (O-PTIR) spectroscopy and imaging (Kansiz et al., 2020; Xia et al., 2022), a new modality of infrared spectroscopy with growing numbers of publications since 2020 (Bakir et al., 2020; Böke et al., 2022; Bouzy et al., 2023; Klementieva et al., 2020; Shaik et al., 2023; Yang et al., 2024). Briefly, the underlying principle of this method involves the use a 532 nm (green) detection laser colinearly aligned with a pulsed infrared tunable quantum cascade laser (QCL), which are focused on the sample surface. The QCL is pulsed onto a ~10 μm spot size, exciting molecular vibrations and leading to a photothermal response, which is monitored by the green laser at a ~500 nm spot size at the center of the ~10-μm region. With this strategy, O-PTIR imaging overcomes the infrared diffraction limit and enables to obtain compositional imaging at an unprecedented submicron resolution.

A great advantage of O-PTIR imaging compared to conventional FTIR spectroscopic methods is that it can achieve data collection at the high spatial resolution of 500 nm with minimal sample preparation, and in non-contact reflection mode. For bone research, this indicates the possibility to assess tissue composition at the submicron scale of the building blocks of bone tissue (Ahn et al., 2022; Reiner et al., 2023). Additionally, this approach enables analysis of thick and intact bone samples without the need for cumbersome and challenging thin sectioning of calcified bone, which is of great practical value. Advancing application of O-PTIR spectroscopy and imaging to investigate bone properties may contribute to fill an important gap in revealing bone submicron scale composition in a variety of samples, including samples for assessment of skeletal diseases and therapeutic interventions.

Another gap in current bone research is the paucity of studies using multivariate approaches to investigate the combined role of compositional tissue-level properties in bone health (Reiner et al., 2023; Abraham et al., 2015; Dragomir-Daescu et al., 2018; Johannesdottir et al., 2017). As bone quality and strength are determined by a combination of underlying factors (Felsenberg and Boonen, 2005; Friedman, 2006), advanced analytical methods are necessary to reveal the multifactorial relationship between bone tissue properties and bone health. Interestingly, recent advancements in machine learning have been applied to bone disease research (Smets et al., 2021). Machine learning is a technology for effecting non-linear regressions between complex data elements (Xu and Jackson, 2019; Greener et al., 2022). For example, a typical application in biomedicine might be predicting heart attacks based on input data from vital signs and medical history. In research on bone fragility in osteoporosis, machine learning has shown great potential for bone properties assessment, diagnosis, fracture detection, and risk prediction (Smets et al., 2021). Studies on bone properties have involved bone mineral density (BMD) (González et al., 2018; Mohamed et al., 2019; Zhang et al., 2019), microarchitecture parameters (Mohanty et al., 2019; Xiao et al., 2020), vertebral fracture load (Zhang et al., 2019), and vertebral height (Pang et al., 2019), with the ultimate goal of improving detection of bone fragility biomarkers.

Here, our first goal was to establish the novel application of O-PTIR spectroscopy and imaging to assess bone submicron composition in thick samples embedded in poly(methyl methacrylate) (PMMA) blocks. Our second goal was to explore the application of machine learning to identify typical and fragile bone phenotypes based on their multivariate tissue-level spectral data. Our overall hypotheses are that (1) O-PTIR will enable imaging bone tissue composition at superior spatial resolution than of conventional FTIR imaging, and (2) machine learning models utilizing O-PTIR spectra as input will accurately predict the bone fragility phenotype seen in a murine model of OI.

Materials and methods

Bone samples

All bones used in this study were female mouse tibias embedded in PMMA, obtained from a separate IACUC-approved study at the Hospital of Special Surgery (HSS) in New York, NY. Bones with "typical" phenotype were harvested from wildtype (WT) animals (n = 6), whereas bones with a "fragile" phenotype were collected from a mouse model of OI (OIM, n = 7), which is characterized by reduced or structurally defective collagen formation, leading to impaired bone mineralization and increased bone fragility and fractures (Alcorta-Sevillano et al., 2023; Chipman et al., 1993). Briefly, WT (+/+) and homozygous OIM (*oim/oim*) mice were obtained from Jackson labs and sacrificed at 26 weeks of age. Tibiae were harvested, cleaned of surrounding soft tissue, fixed in 100 % ethanol, and embedded in PMMA. The blocks were then cut into 2–4 mm thick segments to expose the bone surface, either longitudinally or across the mid-diaphysis, using a IsoMet 100 Precision Saw (Buehler).

O-PTIR imaging and spectroscopy

Spectral images of the exposed bone surface were obtained in a mIRage sub-micron infrared microscope (Photothermal Spectroscopy Corp.), which uses a quantum cascade laser (QCL) source and a 532 nm visible probe. Images were collected using 500 nm step size, 1030 cm^{-1} as reference frequency, 44 % IR power, 0.5 % laser power, and avalanche photodiode detector (APD). Single-wavenumber images were acquired at specific frequencies to visualize the distribution of PMMA, mineral, and protein (1735, 1030, and 1650 cm^{-1}, respectively). The images were processed using PTIR Studio software (Photothermal Spectroscopy Corp.) to obtained RGB overlays highlighting the co-distribution of different components, as well as the ratio of the mineral image to the PMMA image (mineral/PMMA), which shows the distribution of mineral content normalized to that of PMMA and enhances the visualization of tissue microporosity.

For assessment of the submicron tissue composition in WT and OIM samples, we used block segments cut cross-sectionally at the tibial mid-diaphysis. Spectra were collected as linescans across the cortical bone, at every 500 nm from the endosteum to the periosteum. Three linescans were acquired per sample, with each linescan resulting in ~150–250 spectra. The spectra from each linescan were then divided into three regions of cortical bone: 20 % for the endosteal region (ER), 60 % for the middle region (MR), and 20 % for the periosteal region (PR). Spectra with large PMMA contribution (collected from the pores across the cortical bone) were excluded when the intensity of the acrylate peak at 1735 cm^{-1} was more than half of the amide I peak at 1660 cm^{-1} (Suppl. Fig. 1a). This process typically removed ~5–8 % of spectra from each sample.

The spectra were preprocessed using the PLS_Toolbox chemometrics software (Eigenvector Research Inc.) within MATLAB by application of Savitsky-Golay smoothing and second derivative filters to enhance and resolve spectral peaks. The intensities of peaks of interest were assessed based on their inverted second derivative heights (Y-axis values), followed by quantification of peak ratios that reflect mineral content relative to protein (1030/1650 cm^{-1}), mineral crystallinity (1030/1020 cm^{-1}), and mineral carbonate content relative to phosphate (875/1030 cm^{-1}) (Querido et al., 2021). Finally, the interquartile range (IQR) method was employed to identify and eliminate outliers within each

dataset; outliers were considered when values were 1.5 × IQR above the third quartile (Q3) or below the first quartile (Q1) (Suppl. Fig. 1b). This process typically removed ~3–7 % of data for the 1030/1650 ratio, ~6–13 % of data for the 1030/1020 ratio, and ~2–6 % of data for the 875/1030 ratio. Means and standard deviations were calculated for each animal, and data comparison between WT (n = 6) and OIM (n = 7) tissues was carried out on Prism software (GraphPad) using a Kruskal–Wallis followed by Dunn's test with statistical significance defined at $p < 0.05$.

Scanning electron microscopy

Visualization of the structure and microporosity of the same samples analyzed by O-PTIR imaging was carried out by scanning electron microscopy (SEM) in a FEI Quanta 450FEG in low-vacuum mode. Settings for image acquisition were: accelerating voltage at 10 kV, working distance at 10 mm, spot size at 4, and dwell time at 10 μs, using electron backscattered detectors.

FTIR imaging

PMMA-embedded bone samples were sectioned at 4 μm thickness and deposited onto BaF_2 optical windows as part of a separate study at the HSS. Standard FTIR images were obtained using a Spotlight 400 (PerkinElmer) in transmission mode, with 4 cm^{-1} spectral resolution, 2 co-added scans, and either 25 μm or 6.25 μm pixel resolution. Images were analyzed using the ISys 5.0 chemical imaging analysis software (Malvern Instruments), to visualize the distribution of specific samples components (PMMA, mineral, and protein) based on the raw spectra intensity of their corresponding peaks (1735, 1030, and 1650 cm^{-1}, respectively). The ratio of the mineral image to the PMMA image (mineral/PMMA) was also obtained.

Machine learning

Analysis was carried out using the second derivative of the O-PTIR spectra collected from WT and OIM samples, which sum a total of ~8300 spectra with 501 variables (wavenumbers) each. The distribution of the first principal components of spectra from each of the mice overlap greatly, and are therefore similar enough to combine together as we have done in this study (Suppl. Fig. 2). For analysis, three spectral ranges were considered: whole range (1800–800 cm^{-1}), collagen range (1800–1200 cm^{-1}, comprising primarily protein peaks), and apatite range (1200–800 cm^{-1}, comprising primarily mineral peaks). Principal component analysis (PCA) was initially performed using The Unscrambler software (CAMO) to visualize the distribution and separation of WT and OIM data based on their scores plot. The spectral data were then reduced using PCA with dimension n = 3. The PC-reduced data were clustered using a support vector machine (SVM) using a radial basis function (RBF) kernel. The RBF kernel projects the points into a higher dimensional space computed as a decaying exponential of the distances between pairs of points. The SVM then computes an optimal hyperdimensional linear decision boundary. To ensure a weighted and even analysis, SVM training and testing was carried out using the same number of spectra from each mouse (250 spectra randomly selected) and the same number of WT and OIM mice (n = 6). Cross-validation was used to test performance, with a 75/25 train/test split and results averaged over n = 20 iterations. Results were computed as a confusion matrix, showing percentages of WT and OIM samples that were correctly identified.

Results

PMMA-embedded bones in thick sections cut longitudinally could be easily visualized using the O-PTIR microscope in brightfield mode for identification of cortical bones, bone marrow space, and surrounding PMMA (Fig. 1a). O-PTIR spectra from cortical bone showed all typical peaks of bone collagen (Amide I, Amide II, C–H) and apatite (PO_4, CO_3) (Fig. 1b), as expected from a conventional FTIR spectrum (Querido et al., 2021). The main peak of PMMA (acrylate C═O) can be used as a reference point to identify and exclude spectra with large PMMA contribution, as it is the most intense PMMA peak and does not overlap with peaks of mineral and collagen in bone. Observing the same samples by SEM revealed further details of the cortical tissue structure, such as microporosity (Fig. 1c). Spectral imaging highlights the distribution of PMMA and bone mineral and protein components throughout the same region, as well as their co-distribution by visualization of RGB overlays (Fig. 1c). It is interesting to note the distribution of PMMA within the tissue microporosity, as well as the presence of protein in the bone marrow space. The identification of mineralized tissue was very clearly limited to the cortical bone regions. In the overlays, it is possible to identify the periosteal tissue, which comprises protein (seen in red), but no mineral (green, overlaid with red in bone, seen as yellow). These results demonstrate the feasibility of O-PTIR spectroscopy and imaging to assess tissue-level composition of PMMA-embedded bone samples.

Additionally, we noticed that the single-wavenumber mineral image normalized to the PMMA image (mineral/PMMA) could provide a detailed view of bone microporosity (Fig. 2a), which showed great spatial correlation with observations done using SEM (Fig. 2b). Furthermore, it was possible to obtain spectra with submicron spatial resolution from tissue structures of interest, such as in linescans collected at 500 nm step size across a single pore (Fig. 2c). In this example, 100 spectra could be collected within a 50 μm linear region, showing clear differences in the spectra from the bone tissue around the pore and the pore space, which is filled by PMMA. A closer look at spectra from the pore, the edge of the tissue, and the tissue itself further demonstrate that PMMA contributions to the spectra were limited to those within and closely adjacent to the pores, with minimal contribution to spectra of the bone tissue itself (Suppl. Fig. 3). This represents a spatial resolution unattainable by conventional FTIR imaging, opening new avenues for analysis of structure-composition associations in bone tissue.

The advantage in the use of O-PTIR imaging for analysis of thick samples at high spatial resolution may be better appreciated when directly compared to FTIR images, carried out with typical thin sections of mouse bone embedded in PMMA (Suppl. Fig. 4a). It is clear to see in the brightfield image some challenges involved in obtaining thin sections of calcified tissues, such as the presence of numerous folds and artifacts and loss of tissue (Suppl. Fig. 4b). Additionally, it is interesting to note the FTIR images acquired at standard pixel resolutions of 25 μm and 6.25 μm to show the distribution of PMMA, mineral, and protein, as well as the mineral/PMMA ratio (Suppl. Fig. 4c). Although this type of images has great reverence for bone analysis, they simply do not reach the same level of detail as those obtained by O-PTIR imaging at 500 nm spatial resolution. To better illustrate the advantage that this higher resolution can bring, we also acquired O-PTIR images from a thick section of PMMA-embedded mouse bone cut cross-sectionally using different spatial resolution settings (Suppl. Fig. 5). Images acquired using 25 and 6 μm resolution exemplify the typical level of detail achieved by conventional FTIR imaging, where tissue microporosity are blurry and hard to precisely appreciate. On the other hand, images acquired at 3 and 0.5 μm resolution highlight the superiority of O-PTIR resolution to visualize bone microporosity with greater clarity.

In cross-sections of WT and OIM bones, linescans could be easily collected across the cortical bone thickness (Suppl. Fig. 6a), resulting in a rich array of spectra reflecting bone submicron-scale composition throughout endosteal, middle, and periosteal regions (Suppl. Fig. 6b). Quantification of peak ratios from each bone region (Suppl. Fig. 6c) showed variations in differences between WT and OIM across different bone regions. Mineral content, indicative of the relative amount of mineral normalized to the amount of protein, was significantly greater in OIM than WT samples only in the middle and periosteal regions.

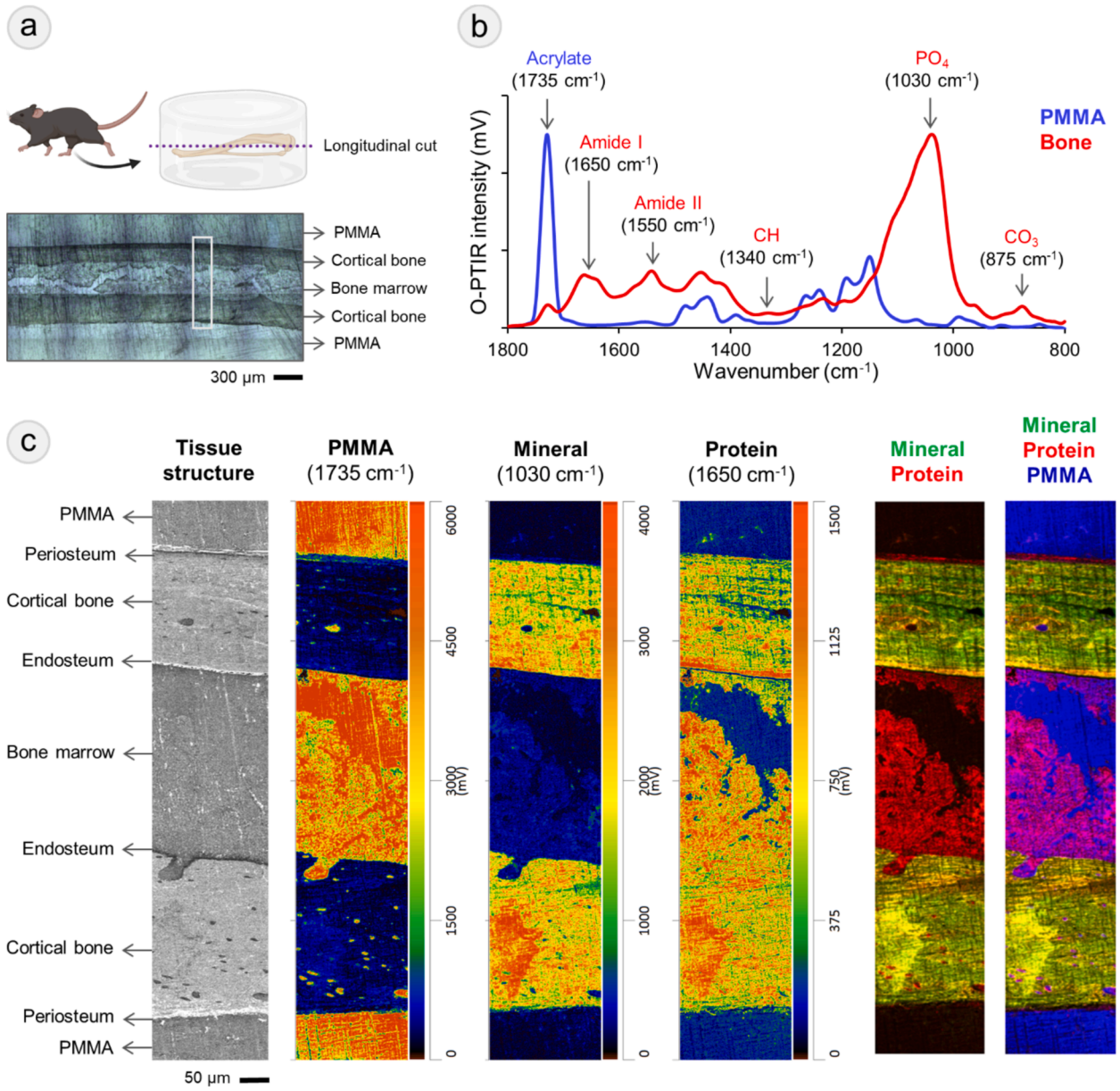

Fig. 1. O-PTIR spectral imaging of PMMA-embedded bone at submicron resolution. (a) Brightfield image of the exposed bone surface in a thick PMMA block cut longitudinally. (b) O-PTIR spectra of cortical bone and PMMA with typical peaks labelled. (c) SEM image of tissue structure and O-PTIR single-wavenumber images of the distribution of PMMA and bone mineral and protein, including RGB overlays.

Additionally, mineral crystallinity, indicative of the maturity and structural order of the mineral, presented generally lower values in OIM samples compared to WT, which was closer to significant in the periosteal region. No significant differences were observed between WT and OIM samples in carbonate content, indicative of the amount of carbonate normalized to the amount of phosphate in the mineral.

Finally, the thousands of spectra collected from WT and OIM bone samples were processed for machine learning analysis, considering different spectral ranges to highlight peaks of collagen or apatite (Fig. 3a). PCA score plots for each spectral range show differences in the separation of spectral data from WT and OIM samples, with a clearer separation obtained considering the collagen range, in contrast to a large data overlap when considering the apatite range (Fig. 3b). Accordingly, SVM models created using the different spectral ranges showed distinct predictive accuracy to identify WT or OIM bone phenotypes based on input of spectral data (Fig. 3c). In particular, 86 % of the WT and 90 % of OIM samples were correctly identified by the model using the collagen range, whereas only 60 % of WT and 81 % of OIM samples were identified correctly using the apatite range. This is an interesting and novel result, which not only corroborates the importance of collagen underlying OI pathogenesis, but also highlights the application of machine learning to distinguish typical and fragile bone phenotypes based on their tissue-level spectral data.

Discussion

We present a new approach to assess the fascinating composition of bone tissue at the submicron level. O-PTIR spectroscopy and imaging is a recent modality of infrared spectroscopy, which has just begun to be explored to assess bone mineralization (Ahn et al., 2022; Reiner et al., 2023). In 2022, Ahn et al. (2022) described the application of O-PTIR spectroscopy to evaluate changes in tissue-level composition along bone aging, noticing that the quantified matrix/mineral ratio decreased as the tissue matured. They also described a larger variation in this spectral

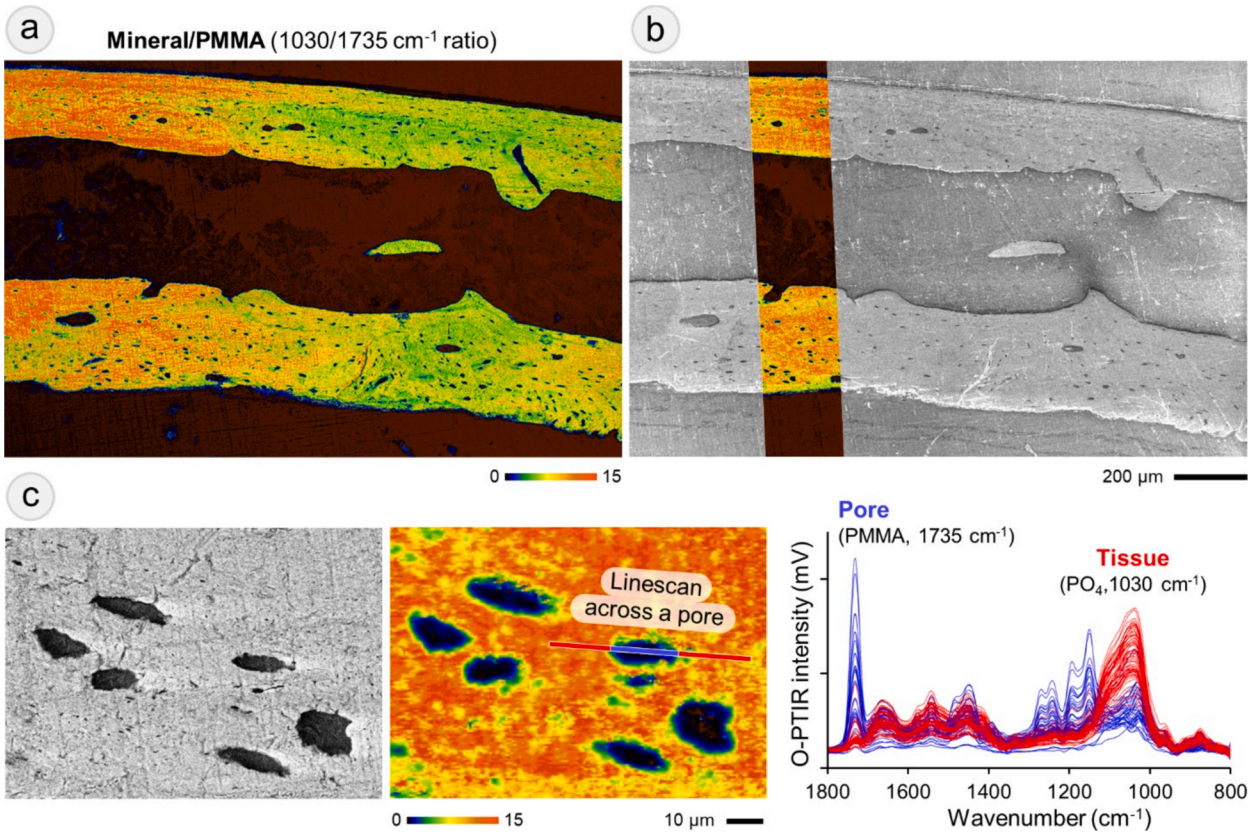

Fig. 2. SEM and O-PTIR images of bone microporosity. (a) O-PTIR image of the mineral/PMMA single-wavenumber image ratio of the exposed cortical bone surface in a thick PMMA block. (b) Overlay of the O-PTIR image of the mineral/PMMA ratio onto the SEM image of the same sample. (c) SEM and O-PTIR image of the same group of micropores, highlighting spectra collected in a linescan across a single pore.

parameter in younger tissue than in older tissues, as well as the presence of wave patterns in the matrix/mineral ratio values progressing from young to mature tissues. In 2023, Reiner et al. (2023) applied O-PTIR spectroscopy to evaluate bone samples subjected to progressive demineralization and thick segments of human cadaveric femur. The authors compared raw spectra, second derivative spectra, and quantified peak ratios obtained by O-PTIR spectroscopy and standard FTIR spectroscopy from the same samples. They showed that the O-PTIR spectral features were typical and comparable to those of FTIR, although some differences between the modalities were noticeable. They showed significant correlations between spectral parameters quantified by both methods, such as mineral content, mineral maturity, and mineral carbonate content, contributing to the ongoing validation of O-PTIR to assess bone tissue compositional properties. Additionally, by using multivariate partial least square regression (PLS) analysis, they showed that combining multiple O-PTIR parameters significantly enhanced prediction of proximal femur stiffness, highlighting the relevance of submicron tissue compositional properties as factors underlying bone mechanical function.

Here, we take a significant step forward by combining two innovative aspects. First, the analysis of bone samples embedded in thick PMMA blocks. This can open a new possibility for assessment of typical PMMA-embedded bone biopsies, without the need for cumbersome thin sectioning of calcified tissue. Second, the application of machine learning for identification of “typical” or “fragile” bones based on their O-PTIR spectral data. This approach shows immense potential towards an automated analysis of spectral data to aid in the evaluation and diagnosis of bone diseases, as well as in assessing changes in bone tissue quality during drug treatments in pre-clinical studies. Additionally, this study highlights the possibility of using O-PTIR images for correlative microscopy. For example, overlaying SEM images of tissue microporosity with O-PTIR images of tissue composition can enable to examine not only how the tissue looks like, but also what are its compositional properties at submicron-scale regions of interest.

We noticed that spectra with large PMMA contributions were limited primarily to those from the pores within the bone tissue. In the spectra of bone tissue itself, the contribution of PMMA was minimal, based on the relative intensity of the acrylate peak at 1735 cm^{-1} to that of amide I peak at 1660 cm^{-1}. Additionally, as shown in Fig. 1b, the main peaks of bone mineral and collagen do not overlap with those of PMMA; thus, unless contamination is excessive, a small contribution of PMMA to bone spectra should not influence quantitative analysis. However, an approach that may be considered in future studies to remove contribution of PMMA is performing standard spectra subtraction (Lebon et al., 2011).

The key to successfully treat prevalent skeletal diseases relies on understanding changes in the tissue leading to reduced bone quality and increased fracture risk. Bone fragility diseases are a major public health problem, affecting hundreds of millions of people worldwide (Clynes et al., 2020; Curtis et al., 2017). Fragility fractures often lead to significant morbidity, mortality, and decreased quality of life, as well as a significant economic burden (Clynes et al., 2020; Curtis et al., 2017). In routine clinical practice, bone mineral density (BMD) is the primary correlate of bone strength used for diagnosis and assessment of fracture risk (Unnanuntana et al., 2010). However, it is well recognized that assessment of BMD alone is a poor predictor of bone strength, and current assessment misses nearly half of individuals at risk of fractures (Jiang et al., 2017; Trémollieres et al., 2010). Analysis of bone biopsies are standard in searching for more detailed diagnosis of bone diseases, such as osteomalacia and osteoporosis, as well as to diagnose osteosarcoma or other types of bone cancer. However, bone histomorphometry is often cumbersome and cannot inform on multiple key compositional

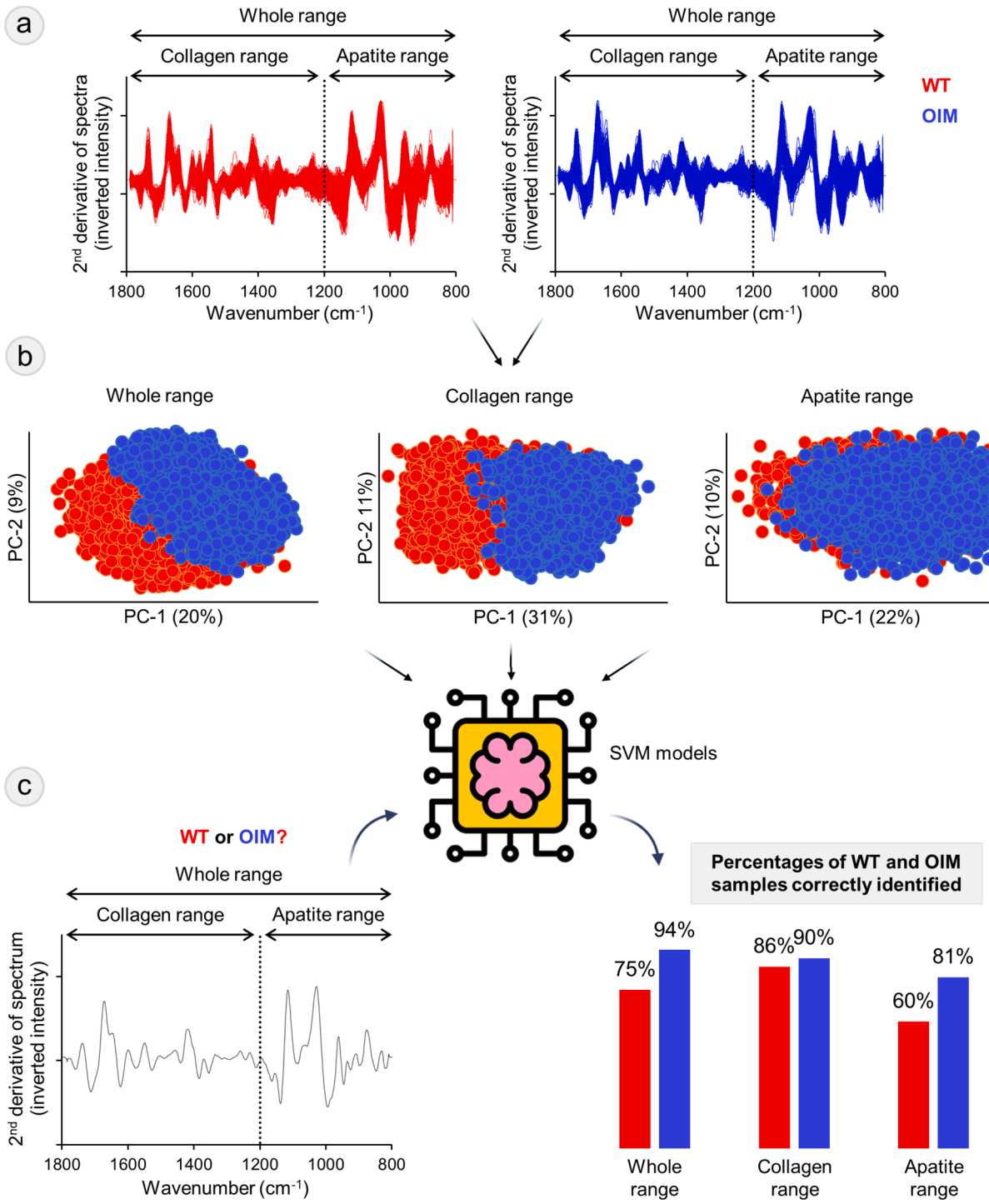

Fig. 3. Machine learning analysis of O-PTIR spectral data of WT and OIM bone samples. (a) 2nd derivative of the spectra (inverted), highlighting spectral ranges comprising peaks of collagen and apatite. (b) PCA score plots obtained using data from different spectral ranges. (c) Development and cross-validation of SVM models (250 spectra per mouse, 6 mice per group; 75/25 train/test split) using each spectral range, highlighting the predictive accuracy of each model to correctly identify WT or OIM phenotypes based on input of spectral data (n = 20 iterations).

properties of bone mineral and matrix. Thus, there is a current need for alternative and adjunct approaches to improve assessment of bone quality, which could aid in diagnosis of bone diseases and more timely and targeted treatment.

FTIR and Raman imaging has been widely used to explore changes in bone tissue composition with disease and drug treatment, as summarized by Taylor and Donnelly (Taylor and Donnelly, 2020). Here, our results are comparable with previous findings obtained using standard analyses of bones from different mouse models of OI. In particular, cortical bone investigations using FTIR imaging (Masci et al., 2016; Boskey et al., 2015; Coleman et al., 2012; Camacho et al., 2003) and Raman spectroscopy (Yao et al., 2013; Bi et al., 2017; Oestreich et al., 2016; Daley et al., 2010) showed that compared to WT, bones from OI animals generally have higher mineral content and unchanged mineral crystallinity and carbonate content. However, it is important to highlight that those previous studies relied primarily on using bulk sample

analysis or imaging at microscale resolution (~6–25 μm pixel resolution). Here, using O-PTIR spectroscopy, we were able to collect spatially defined spectra at 500 nm resolution across different cortical bone regions (endosteal, middle, periosteal). This allowed noticing new region-dependent differences between WT and OIM bones, with more significant differences seen in the periosteal region. Compared to the endosteal region, bone tissue at the periosteal region has lower remodeling activity with bone formation often exceeding resorption, playing key roles in appositional bone growth and fracture repair (Clarke, 2008). Interestingly, mechanical loading strains has been described to be especially prominent on periosteal regions (Turunen et al., 2016; Pereira et al., 2015), highlighting the importance of the periosteal tissue for bone mechanical function. Based on our new findings, it is conceivable that the OI effects on periosteal bone tissue properties may be a key factor underlying pathogenesis and increased bone fragility. This can motivative future studies testing new therapeutics in OI mouse models to focus particularly on how they improve bone quality at the periosteal tissue.

An advantage of achieving this resolution is highlighted in the microporosity images shown here, especially in Suppl. Fig. 5, which shows a direct comparison of images from the same region acquired using different resolutions. It is obvious that to assess detailed features of bone tissue, such as microporosity associated with osteocyte lacuna, the higher resolution achieved using O-PTIR imaging is necessary. For example, an area of active and emergent research has been on the role of osteocytes in directly remodeling their local bone matrix lining the lacuna via perilacunar remodeling (PLR), which changes the material properties of the perilacunar tissue and can affect bone mechanical properties and resistance to fractures (Choi et al., 2021; Qing and Bonewald, 2009; Kegelman et al., 2020; Creecy et al., 2020; Dole et al., 2017; Dole et al., 2021; Sieverts et al., 2024). However, as the perilacunar tissue extends only a few microns from the lacunar wall (Bonivtch et al., 2007; Rux et al., 2022), FTIR imaging cannot adequately assess its composition. Although Raman spectroscopy can achieve a better spatial resolution than FTIR imaging (Taylor and Donnelly, 2020; van der Meijden et al., 2023) and has been applied to investigate the perilacunar matrix (Gardinier et al., 2016; Bolger et al., 2023), the novel application of O-PTIR to provide images of bone composition at submicron resolution may greatly benefit the field by offering an excellent approach to gain new insights into the compositional features of the minute perilacunar tissue, as well as how it is associated with bone disease and fragility.

Additionally, our results using different ranges of the spectral data as input in machine learning models are interesting. Comparing the accuracy of the models in correctly identifying OIM samples based on the collagen range (90 %) or mineral range (81 %) highlights that changes in collagen are more prominent markers underlying the OIM phenotype. As OI is attributable to mutations of type I collagen, our findings are reasonable, and add to the validity of this approach to distinguish and identify bones with different compositional properties based on spectral data. Moreover, these results highlight the multifactorial relationship between tissue-level composition and bone fragility phenotype, which may not be captured using conventional univariate metrics. This is in line with the previous study by Reiner et al. (2023), which described that models for prediction of bone stiffness based on input of combined O-PTIR-derived submicron compositional properties was superior than models using either single properties or combined FTIR properties. Together, these studies support and encourage future research applying multivariate chemometrics and machine learning to elucidate the complex relationship between tissue composition and disease or mechanical function, which will bring new insights into mechanisms and underlying factors of bone fragility. Future research is necessary to investigate whether machine learning predictions using O-PTIR submicron-scale data differs from those using standard FTIR micron-scale data of the same samples, which may further contribute to understanding the role of bone matrix composition at different length scales to bone quality and strength.

O-PTIR imaging has remarkable advantages; however, it also has limitations. One of them is that it requires long acquisition times for hyperspectral imaging at high 500-nm resolution. For example, imaging a 30 × 30 μm area can take ~20 h depending on the settings. The system does offer options for single-wavenumber imaging, which are much faster than hyperspectral; imaging for example the distribution of PMMA and mineral in the same 30 × 30 μm area takes only a couple of minutes. In this case, each image is created based on the intensity of the raw spectral frequencies at 1735 and 1030 cm^{-1}, respectively. Although this is a great approach, a few details need to be considered, especially when pursuing quantitative assessment of peak ratio images. First, O-PTIR imaging in reflection mode is overly sensitive to focus of the green laser on the sample surface, and single-wavenumber imaging of slightly rough or slanted samples often leads to artifacts, in our experience. This can be overcome by polishing and/or selecting smaller areas to image where the focus is similar throughout the surface. Second, quantitative assessment based on the ratio between two single-wavenumber images should be done with care, as each image reflects the height (Y-axis value) of the raw peak, with no spectral processing applied. This is important because established approaches to quantify compositional tissue properties based on infrared spectra primarily involves spectral processing and calculation of peak intensities as areas or second derivative peak heights (Taylor and Donnelly, 2020; Boskey and Camacho, 2007; Querido et al., 2021); thus, assessment of the single-wavenumber raw intensity ratio may need to be further validated for reliable quantitative analysis.

Our study demonstrates the novel application of O-PTIR spectroscopy and imaging to assess bone tissue composition with submicron spatial resolution in thick embedded samples. Moreover, machine learning analysis highlights the potential of this approach to use tissue-level spectral data to identify fragile bones at risk of fracture. In particular, this method may be of value for the analysis of samples from animals in pre-clinical studies on the effects of new therapeutic interventions for skeletal diseases and typical bone biopsies from individuals under examination for diseases, such as osteoporosis, osteomalacia, and bone cancer. Research on this field may greatly contribute to elucidate the role of bone submicron composition underlying skeletal diseases, as well as offer a new perspective to improve diagnosis and the design of optimized treatment strategies. Further applications of O-PTIR spectroscopy and imaging combined with machine and deep learning analysis may offer an innovative approach to investigate mineralized tissues across disciplines (bone biology, orthopedics, dental, archeology, paleontology, forensics).

Declaration of competing interest

The authors declare that they have no known competing financial interests or personal relationships that could have appeared to influence the work reported in this paper.

Acknowledgements

This research was supported by NIH/NIAMS award R21AR082129. Bone samples were kindly provided by the HSS in New York, NY. We thank Frank Weston (Photothermal Spectroscopy Corp.) for his assistance and expertise in O-PTIR spectroscopy and imaging analysis.

Appendix A. Supplementary material

Supplementary material to this article can be found online at https://doi.org/10.1016/j.yjsbx.2024.100111.

References

Abel, R.L., Stavri, R., Gray, M., Hansen, U., 2021. Clinical importance of bone matrix damage mechanisms for fracture prevention. Curr. Osteoporos. Rep. 19 (3), 318–326.

Abraham, A.C., Agarwalla, A., Yadavalli, A., McAndrew, C., Liu, J.Y., Tang, S.Y., 2015. Multiscale predictors of femoral neck in situ strength in aging women: Contributions of BMD, cortical porosity, reference point indentation, and nonenzymatic glycation. J. Bone Miner. Res. 30 (12), 2207–2214.

Ahn, T., Jueckstock, M., Mandair, G.S., Henderson, J., Sinder, B.P., Kozloff, K.M., Banaszak Holl, M.M., 2022. Matrix/mineral ratio and domain size variation with bone tissue age: A photothermal infrared study. J. Struct. Biol. 214 (3), 107878.

Alcorta-Sevillano, N., Infante, A., Macías, I., Rodríguez, C.I., 2023. Murine animal models in osteogenesis imperfecta: The quest for improving the quality of life. Int. J. Mol. Sci. 24 (1). https://doi.org/10.3390/ijms24010184.

Baker, M.J., Trevisan, J., Bassan, P., Bhargava, R., Butler, H.J., Dorling, K.M., Fielden, P. R., Fogarty, S.W., Fullwood, N.J., Heys, K.A., et al., 2014. Using Fourier transform IR spectroscopy to analyze biological materials. Nat. Protoc. 9 (8), 1771–1791.

Bakir, G., Girouard, B.E., Wiens, R., Mastel, S., Dillon, E., Kansiz, M., Gough, K.M., 2020. Orientation matters: Polarization dependent IR spectroscopy of collagen from intact tendon down to the single fibril level. Molecules 25 (18).

Balan, V., Mihai, C.T., Cojocaru, F.D., Uritu, C.M., Dodi, G., Botezat, D., Gardikiotis, I., 2019. Vibrational spectroscopy fingerprinting in medicine: From molecular to clinical practice. Materials (Basel) 12 (18).

Bi, X., Grafe, I., Ding, H., Flores, R., Munivez, E., Jiang, M.M., Dawson, B., Lee, B., Ambrose, C.G., 2017. Correlations between bone mechanical properties and bone composition parameters in mouse models of dominant and recessive osteogenesis imperfecta and the response to anti-TGF-β treatment. J. Bone Miner. Res. 32 (2), 347–359.

Böke, J.S., Popp, J., Krafft, C., 2022. Optical photothermal infrared spectroscopy with simultaneously acquired Raman spectroscopy for two-dimensional microplastic identification. Sci. Rep. 12 (1), 18785.

Bolger, M.W., Tekkey, T., Kohn, D.H., 2023. The contribution of perilacunar composition and mechanical properties to whole-bone mechanical outcomes in streptozotocin-induced diabetes. Calcif. Tissue Int. 113 (2), 229–245.

Bonivtch, A.R., Bonewald, L.F., Nicolella, D.P., 2007. Tissue strain amplification at the osteocyte lacuna: A microstructural finite element analysis. J. Biomech. 40 (10), 2199–2206.

Boskey, A.L., 2013. Bone composition: Relationship to bone fragility and antiosteoporotic drug effects. Bonekey Rep. 2, 447.

Boskey, A., Camacho, N.P., 2007. FT-IR imaging of native and tissue-engineered bone and cartilage. Biomaterials 28 (15), 2465–2478.

Boskey, A.L., Imbert, L., 2017. Bone quality changes associated with aging and disease: A review. Ann. N. Y. Acad. Sci. 1410 (1), 93–106.

Boskey, A.L., Marino, J., Spevak, L., Pleshko, N., Doty, S., Carter, E.M., Raggio, C.L., 2015. Are changes in composition in response to treatment of a mouse model of osteogenesis imperfecta sex-dependent? Clin. Orthop. Relat. Res. 473 (8), 2587–2598.

Bouzy, P., Lyburn, I.D., Pinder, S.E., Scott, R., Mansfield, J., Moger, J., Greenwood, C., Bouybayoune, I., Cornford, E., Rogers, K., et al., 2023. Exploration of utility of combined optical photothermal infrared and Raman imaging for investigating the chemical composition of microcalcifications in breast cancer. Anal. Methods 15 (13), 1620–1630.

Buss, D.J., Kröger, R., McKee, M.D., Reznikov, N., 2022. Hierarchical organization of bone in three dimensions: A twist of twists. J. Struct. Biol. X 6, 100057.

Camacho, N.P., Carroll, P., Raggio, C.L., 2003. Fourier transform infrared imaging spectroscopy (FT-IRIS) of mineralization in bisphosphonate-treated OIM/OIM mice. Calcif. Tissue Int. 72 (5), 604–609.

Chipman, S.D., Sweet, H.O., McBride, D.J., Davisson, M.T., Marks, S.C., Shuldiner, A.R., Wenstrup, R.J., Rowe, D.W., Shapiro, J.R., 1993. Defective pro alpha 2(i) collagen synthesis in a recessive mutation in mice: A model of human osteogenesis imperfecta. Proc. Natl. Acad. Sci. 90 (5), 1701–1705.

Choi, J.U.A., Kijas, A.W., Lauko, J., Rowan, A.E., 2021. The mechanosensory role of osteocytes and implications for bone health and disease states. Front. Cell Dev. Biol. 9, 770143.

Clarke, B., 2008. Normal bone anatomy and physiology. Clin. J. Am. Soc. Nephrol. 3 (Suppl 3), S131–S139.

Clynes, M.A., Harvey, N.C., Curtis, E.M., Fuggle, N.R., Dennison, E.M., Cooper, C., 2020. The epidemiology of osteoporosis. Br. Med. Bull. 133 (1), 105–117.

Coleman, R.M., Aguilera, L., Quinones, L., Lukashova, L., Poirier, C., Boskey, A., 2012. Comparison of bone tissue properties in mouse models with collagenous and non-collagenous genetic mutations using FTIRI. Bone 51 (5), 920–928.

Creecy, A., Damrath, J.G., Wallace, J.M., 2020. Control of bone matrix properties by osteocytes. Front. Endocrinol. (Lausanne) 11, 578477.

Curtis, E.M., Moon, R.J., Harvey, N.C., Cooper, C., 2017. The impact of fragility fracture and approaches to osteoporosis risk assessment worldwide. Bone 104, 29–38.

Daley, E., Streeten, E.A., Sorkin, J.D., Kuznetsova, N., Shapses, S.A., Carleton, S.M., Shuldiner, A.R., Marini, J.C., Phillips, C.L., Goldstein, S.A., et al., 2010. Variable bone fragility associated with an amish col1a2 variant and a knock-in mouse model. J. Bone Miner. Res. 25 (2), 247–261.

Dole, N.S., Mazur, C.M., Acevedo, C., Lopez, J.P., Monteiro, D.A., Fowler, T.W., Gludovatz, B., Walsh, F., Regan, J.N., Messina, S., et al., 2017. Osteocyte-intrinsic TGF-β signaling regulates bone quality through perilacunar/canalicular remodeling. Cell Rep. 21 (9), 2585–2596.

Dole, N.S., Yee, C.S., Schurman, C.A., Dallas, S.L., Alliston, T., 2021. Assessment of osteocytes: Techniques for studying morphological and molecular changes associated with perilacunar/canalicular remodeling of the bone matrix. Methods Mol. Biol. 2230, 303–323.

Dragomir-Daescu, D., Rossman, T.L., Rezaei, A., Carlson, K.D., Kallmes, D.F., Skinner, J. A., Khosla, S., Amin, S., 2018. Factors associated with proximal femur fracture determined in a large cadaveric cohort. Bone 116, 196–202.

Felsenberg, D., Boonen, S., 2005. The bone quality framework: Determinants of bone strength and their interrelationships, and implications for osteoporosis management. Clin. Ther. 27 (1), 1–11.

Friedman, A.W., 2006. Important determinants of bone strength: Beyond bone mineral density. J. Clin. Rheumatol. 12 (2), 70–77.

Garcia-Giner, V., Han, Z., Giuliani, F., Porter, A.E., 2021. Nanoscale imaging and analysis of bone pathologies. Appl. Sci. 11 (24).

Gardinier, J.D., Al-Omaishi, S., Morris, M.D., Kohn, D.H., 2016. PTH signaling mediates perilacunar remodeling during exercise. Matrix Biol. 52–54, 162–175.

González, G., Washko, G.R., Estépar, R.S.J., 2018. Deep learning for biomarker regression: Application to osteoporosis and emphysema on chest CT scans. In: Proc. SPIE Int. Soc. Opt. Eng., p. 10574.

Greener, J.G., Kandathil, S.M., Moffat, L., Jones, D.T., 2022. A guide to machine learning for biologists. Nat. Rev. Mol. Cell Biol. 23 (1), 40–55.

Jiang, X., Gruner, M., Trémollieres, F., Pluskiewicz, W., Sornay-Rendu, E., Adamczyk, P., Schnatz, P.F., 2017. Diagnostic accuracy of FRAX in predicting the 10-year risk of osteoporotic fractures using the USA treatment thresholds: A systematic review and meta-analysis. Bone 99, 20–25.

Johannesdottir, F., Thrall, E., Muller, J., Keaveny, T.M., Kopperdahl, D.L., Bouxsein, M. L., 2017. Comparison of non-invasive assessments of strength of the proximal femur. Bone 105, 93–102.

Kansiz, M., Prater, C., Dillon, E., Lo, M., Anderson, J., Marcott, C., Demissie, A., Chen, Y., Kunkel, G., 2020. Optical photothermal infrared microspectroscopy with simultaneous Raman – A new non-contact failure analysis technique for identification of <10 μm organic contamination in the hard drive and other electronics industries. Micros. Today 28 (3), 26–36.

Kegelman, C.D., Coulombe, J.C., Jordan, K.M., Horan, D.J., Qin, L., Robling, A.G., Ferguson, V.L., Bellido, T.M., Boerckel, J.D., 2020. Yap and TAZ mediate osteocyte perilacunar/canalicular remodeling. J. Bone Miner. Res. 35 (1), 196–210.

Klementieva, O., Sandt, C., Martinsson, I., Kansiz, M., Gouras, G.K., Borondics, F., 2020. Super-resolution infrared imaging of polymorphic amyloid aggregates directly in neurons. Adv. Sci. (Weinh) 7 (6), 1903004.

Lebon, M., Müller, K., Bahain, J.-J., Fröhlich, F., Falguères, C., Bertrand, L., Sandt, C., Reiche, I., 2011. Imaging fossil bone alterations at the microscale by SR-FTIR microspectroscopy. J. Anal. At. Spectrom. 26 (5), 922–929.

Ma, S., Goh, E.L., Tay, T., Wiles, C.C., Boughton, O., Churchwell, J.H., Wu, Y., Karunaratne, A., Bhattacharya, R., Terrill, N., et al., 2020. Nanoscale mechanisms in age-related hip-fractures. Sci. Rep. 10 (1), 14208.

Masci, M., Wang, M., Imbert, L., Barnes, A.M., Spevak, L., Lukashova, L., Huang, Y.H., Ma, Y., Marini, J.C., Jacobsen, C.M., et al., 2016. Bone mineral properties in growing col1a2(+/g610c) mice, an animal model of osteogenesis imperfecta. Bone 87, 120–129.

Mohamed, E.I., Meshref, R.A., Abdel-Mageed, S.M., Moustafa, M.H., Badawi, M.I., Darwish, S.H., 2019. A novel morphological analysis of DXA-DICOM images by artificial neural networks for estimating bone mineral density in health and disease. J. Clin. Densitom. 22 (3), 382–390.

Mohanty, K., Yousefian, O., Karbalaeisadegh, Y., Ulrich, M., Grimal, Q., Muller, M., 2019. Artificial neural network to estimate micro-architectural properties of cortical bone using ultrasonic attenuation: A 2-d numerical study. Comput. Biol. Med. 114, 103457.

Oestreich, A.K., Carleton, S.M., Yao, X., Gentry, B.A., Raw, C.E., Brown, M., Pfeiffer, F. M., Wang, Y., Phillips, C.L., 2016. Myostatin deficiency partially rescues the bone phenotype of osteogenesis imperfecta model mice. Osteoporos. Int. 27 (1), 161–170.

Pang, S., Su, Z., Leung, S., Nachum, I.B., Chen, B., Feng, Q., Li, S., 2019. Direct automated quantitative measurement of spine by cascade amplifier regression network with manifold regularization. Med. Image Anal. 55, 103–115.

Pereira, A.F., Javaheri, B., Pitsillides, A.A., Shefelbine, S.J., 2015. Predicting cortical bone adaptation to axial loading in the mouse tibia. J. R. Soc. Interface 12 (110), 0590.

Qian, T., Chen, X., Hang, F., 2020. Investigation of nanoscale failure behaviour of cortical bone under stress by AFM. J. Mech. Behav. Biomed. Mater. 112, 103989.

Qing, H., Bonewald, L.F., 2009. Osteocyte remodeling of the perilacunar and pericanalicular matrix. Int. J. Oral Sci. 1 (2), 59–65.

Querido, W., Kandel, S., Pleshko, N., 2021. Applications of vibrational spectroscopy for analysis of connective tissues. Molecules 26 (4).

Reiner, E., Weston, F., Pleshko, N., Querido, W., 2023. Application of optical photothermal infrared (O-PTIR) spectroscopy for assessment of bone composition at the submicron scale. Appl. Spectrosc., 37028231201427

Rux, C.J., Vahidi, G., Darabi, A., Cox, L.M., Heveran, C.M., 2022. Perilacunar bone tissue exhibits sub-micrometer modulus gradation which depends on the recency of osteocyte bone formation in both young adult and early-old-age female c57bl/6 mice. Bone 157, 116327.

Sabet, F.A., Raeisi Najafi, A., Hamed, E., Jasiuk, I., 2016. Modelling of bone fracture and strength at different length scales: A review. Interface Focus 6 (1), 20150055.

Shaik, T.A., Ramoji, A., Milis, N., Popp, J., Krafft, C., 2023. Optical photothermal infrared spectroscopy and discrete wavenumber imaging for high content screening of single cells. Analyst 148 (22), 5627–5635.

Sieverts, M., Yee, C., Nemani, M., Parkinson, D.Y., Alliston, T., Acevedo, C., 2024. Spatial control of perilacunar canalicular remodeling during lactation. Sci. Rep. 14 (1), 14655.

Smets, J., Shevroja, E., Hügle, T., Leslie, W.D., Hans, D., 2021. Machine learning solutions for osteoporosis-a review. J. Bone Miner. Res. 36 (5), 833–851.
Tai, K., Dao, M., Suresh, S., Palazoglu, A., Ortiz, C., 2007. Nanoscale heterogeneity promotes energy dissipation in bone. Nat. Mater. 6 (6), 454–462.
Taylor, E.A., Donnelly, E., 2020. Raman and Fourier transform infrared imaging for characterization of bone material properties. Bone 139, 115490.
Trémollieres, F.A., Pouillès, J.M., Drewniak, N., Laparra, J., Ribot, C.A., Dargent-Molina, P., 2010. Fracture risk prediction using BMD and clinical risk factors in early postmenopausal women: Sensitivity of the WHO FRAX tool. J. Bone Miner. Res. 25 (5), 1002–1009.
Turunen, M.J., Kaspersen, J.D., Olsson, U., Guizar-Sicairos, M., Bech, M., Schaff, F., Tägil, M., Jurvelin, J.S., Isaksson, H., 2016. Bone mineral crystal size and organization vary across mature rat bone cortex. J. Struct. Biol. 195 (3), 337–344.
Unnanuntana, A., Gladnick, B.P., Donnelly, E., Lane, J.M., 2010. The assessment of fracture risk. J. Bone Joint Surg. Am. 92 (3), 743–753.
van der Meijden, R.H.M., Daviran, D., Rutten, L., Walboomers, X.F., Macías-Sánchez, E., Sommerdijk, N., Akiva, A., 2023. A 3D cell-free bone model shows collagen mineralization is driven and controlled by the matrix. Adv. Funct. Mater. 33 (42), 2212339.
Xia, Q., Yin, J., Guo, Z., Cheng, J.X., 2022. Mid-infrared photothermal microscopy: Principle, instrumentation, and applications. J. Phys. Chem. B 126 (43), 8597–8613.
Xiao, P., Zhang, T., Dong, X.N., Han, Y., Huang, Y., Wang, X., 2020. Prediction of trabecular bone architectural features by deep learning models using simulated DXA images. Bone Rep. 13, 100295.
Xu, C., Jackson, S.A., 2019. Machine learning and complex biological data. Genome Biol. 20 (1), 76.
Yang, C., Xie, J., Gowen, A., Xu, J.L., 2024. Machine learning driven methodology for enhanced nylon microplastic detection and characterization. Sci. Rep. 14 (1), 3464.
Yao, X., Carleton, S.M., Kettle, A.D., Melander, J., Phillips, C.L., Wang, Y., 2013. Gender-dependence of bone structure and properties in adult osteogenesis imperfecta murine model. Ann. Biomed. Eng. 41 (6), 1139–1149.
Zhang, M., Gong, H., Zhang, K., 2019. Prediction of lumbar vertebral strength of elderly men based on quantitative computed tomography images using machine learning. Osteoporos. Int. 30 (11), 2271–2282.
Zhang, T., Liu, P., Zhang, Y., Wang, W., Lu, Y., Xi, M., Duan, S., Guan, F., 2019. Combining information from multiple bone turnover markers as diagnostic indices for osteoporosis using support vector machines. Biomarkers 24 (2), 120–126.
Zimmermann, E.A., Schaible, E., Bale, H., Barth, H.D., Tang, S.Y., Reichert, P., Busse, B., Alliston, T., Ager, J.W., Ritchie, R.O., 2011. Age-related changes in the plasticity and toughness of human cortical bone at multiple length scales. PNAS 108 (35), 14416–14421.